Highly active Pd containing EMT zeolite catalyst for indirect oxidative carbonylation of methanol to dimethyl carbonate

Chunzheng Wang, Weisong Xu, Zhengxing Qin, Hailing Guo, Xinmei Liu, Svetlana Mintova

▶ **To cite this version:**

Chunzheng Wang, Weisong Xu, Zhengxing Qin, Hailing Guo, Xinmei Liu, et al.. Highly active Pd containing EMT zeolite catalyst for indirect oxidative carbonylation of methanol to dimethyl carbonate. Journal of Energy Chemistry, 2021, 52, pp.191-201. 10.1016/j.jechem.2020.04.045 . hal-02893798

HAL Id: hal-02893798
https://hal.science/hal-02893798

Submitted on 27 Nov 2020

HAL is a multi-disciplinary open access archive for the deposit and dissemination of scientific research documents, whether they are published or not. The documents may come from teaching and research institutions in France or abroad, or from public or private research centers.

L'archive ouverte pluridisciplinaire **HAL**, est destinée au dépôt et à la diffusion de documents scientifiques de niveau recherche, publiés ou non, émanant des établissements d'enseignement et de recherche français ou étrangers, des laboratoires publics ou privés.

Highly active Pd containing EMT zeolite catalyst for indirect oxidative carbonylation of methanol to dimethyl carbonate

Chunzheng Wang[a], Weisong Xu[a], Zhengxing Qin[a], Hailing Guo[a], Xinmei Liu[a,*], Svetlana Mintova[a,b,*]

[a] State Key Laboratory of Heavy Oil Processing, College of Chemical Engineering, China University of Petroleum (East China), Qingdao 266580, China

[b] Laboratoire Catalyse et Spectrochimie (LCS), Normandie Université, ENSICAEN, UNICAEN, CNRS, 6 boulevard Maréchal Juin, Caen 14050, France

[*] Corresponding authors. E-mail: *lxmei@upc.edu.cn (X. Liu), svetlana.mintova@ensicaen.fr (S. Mintova)*

Abstract

Palladium containing EMT zeolite catalyst (Pd/EMT) was prepared and used for the indirect oxidative carbonylation of methanol to dimethyl carbonate (DMC). The EMT zeolite was employed as a new catalyst support and compared with the conventional Pd containing FAU zeolite catalyst (Pd/FAU). The Pd/EMT in contrast to the Pd/FAU catalyst exhibited high intrinsic activity with the turnover frequency of 0.25 s^{-1} *vs.* 0.11 s^{-1}. The Pd/EMT catalyst showed high CO conversion of 82% and DMC selectivity of 79%, that maintained for at least 130 h, while the activity of the Pd/FAU catalyst rapidly deteriorated within 12 h. The enhanced interactions between Pd and EMT zeolite inhibited the sintering of palladium clusters and maintained the Pd^{2+} active sites in the Pd/EMT catalyst. The stabilization of the mono-dispersed Pd clusters within the EMT zeolite is paramount to the excellent performance of the catalyst for the indirect oxidative carbonylation of methanol to DMC.

Keywords: EMT; Palladium; Stability; Carbonylation; Dimethyl carbonate

1. Introduction

Dimethyl carbonate (DMC) is an environmentally sustainable compound with useful and versatile chemical properties [1,2]. DMC can serve as a green carbonylation and methylation reagent in place of toxic phosgene and dimethyl sulfate [3]. The high oxygen content (53 wt. %) of DMC and rapid biodegradability make it a promising gasoline additive [4]. DMC is also used as an effective solvent for organic synthesis, coating and electrolyte in lithium ion batteries, and as a common monomer for the production of polycarbonate [5]. The traditional production of DMC ($(CH_3O)_2CO$) is based on the reaction of phosgene ($COCl_2$) with methanol (CH_3OH) via methyl chloroformate; the extreme toxicity of $COCl_2$ and serious equipment corrosion caused by hydrogen chloride byproduct are of major concern [6]. Recently, great efforts have been made to develop green chemical routes for DMC production including [7–9]: (1) the direct oxidative carbonylation of carbon monoxide (CO), oxygen (O_2) and CH_3OH; (2) the indirect oxidative carbonylation of CO, O_2 and CH_3OH; (3) the direct synthesis from carbon dioxide (CO_2) and CH_3OH; (4) the methanolysis of urea; and (5) the transesterification of ethylene/propylene carbonate with CH_3OH. Among these processes, the indirect oxidative carbonylation of methanol to DMC is considered to be an ambitious route because of the mild reaction conditions, high atom efficiency and low cost [10]. This indirect route for DMC synthesis involves two separate reactions (Scheme S1 in Supporting Information (SI)): (1) non-catalytic synthesis of methyl nitrite (CH_3ONO) with CH_3OH and O_2: $2\ CH_3OH + 2\ NO + 1/2\ O_2 \rightarrow 2\ CH_3ONO + H_2O$; (2) Pd-catalyzed oxidative carbonylation to DMC: $CO + 2\ CH_3ONO \rightarrow (CH_3O)_2CO + 2\ NO$ (The formed NO can be recycled for the synthesis of methyl nitrite). The overall reaction ($CO + 2\ CH_3OH + 1/2\ O_2 \rightarrow (CH_3O)_2CO + H_2O$) results in an environmentally benign and highly efficient process.

The Pd-based catalysts used for the indirect oxidative carbonylation of methanol to DMC are either chlorine-containing or chlorine-free catalysts [11–13]. The gas-phase process has been successfully commercialized by Ube Industries, Ltd. (15, 000 tons/year), using a $PdCl_2$/active-carbon catalyst [14,15]. However, chlorine (e.g., 100 μL L^{-1} hydrogen chloride) must be added into the reactants to maintain the activity of the chlorine-containing catalysts [13,15]. The introduction of chlorine leads to the corrosion of equipment, difficult regeneration of chlorine, and unsatisfactory purity of DMC product [13,15], which encounters problems related with the green chemistry concept. Therefore, significant work is dedicated to the development of chlorine-free, high-performance Pd catalysts. Tan et al. found that the activity of Pd/FAU catalyst was improved by increasing the Pd oxidation states [16]. They also revealed, by density functional theory (DFT) calculations, that the Pd^{2+} species was responsible for the formation of DMC while the aggregation of Pd^0 species resulted in the generation of dimethyl oxalate (DMO) byproduct [10]. Dong et al. demonstrated that the potassium promoter improved the electron density of Pd clusters and thus enhanced the activation of CO reactant on the Pd/FAU catalyst; both theoretical and experimental proofs were provided [12]. Guo et al. reported that the Cu-doped Pd/FAU catalyst showed higher activity and selectivity than the Cu-free Pd/FAU catalyst, possibly due to the increased Pd^{2+}/Pd^0 ratio of Pd clusters [17]. It is accepted that Brønsted acidity can accelerate the decomposition of CH_3ONO reactant, and result in poor catalyst selectivity [1]. Dong et al. presented a nearly linear relationship between the turnover frequency (TOF) and the amount of Lewis acidity of the Pd/FAU catalyst [18]. They also suggested that Lewis acid sites could accept electrons from the Pd species and thus promote the formation of electron-deficient Pd^{x+} active sites [18]. The possible mechanism included the adsorption of CH_3ONO on Pd^{2+} actives sites forming $Pd(OCH_3)(NO)$ and the subsequent CO insertion generating the $Pd(COOCH_3)(NO)$; this is coupled

with CH_3ONO to produce DMC [19]. The catalyst stability is of crucial consideration, but as far as we know, the stability was only reported in a few articles [10,19]. Yamamoto et al. [19] found that the DMC yield of Pd/FAU catalyst declined remarkably within 100 h and decreased by about 50% after 300 h test, possibly due to the sintering of Pd clusters. Recently, Tan et al. [10] reported on a stable Pd/FAU catalyst for 100 h, but the selectivity of inevitable byproducts such as methyl formate and dimethoxymethane was not provided. The work reported up to now only focused on the use of FAU zeolite framework as a support [11,13]. Therefore, designing high-performance Pd catalysts by exploring alternative zeolite frameworks and properties is desirable for both fundamental research and commercial application.

Like FAU-type zeolite, the EMT-type zeolite is constituted of sodalite cages linked by double six-rings. The EMT framework structure results from a stacking of faujasite sheets through a mirror plane symmetry while the FAU framework structure is founded through an inversion center symmetry [20,21]. The EMT zeolite possesses two sets of cages, i.e. the hypocage (0.61 nm^3; channel: 0.75 nm × 0.65 nm) and hypercage (1.24 nm^3; channel: 0.73 nm × 0.73 nm) [22,23]. In contrast to the hexagonal EMT zeolite, the cubic FAU has only one type of supercage (1.15 nm^3; channel: 0.74 nm × 0.74 nm). The different topology of EMT and FAU also results in different cation locations and site energies [24,25]. The unique cage structure and cation locations in the EMT zeolite may bring benefits in catalysis [25,26]. Daou et al. [27] found that the EMT zeolite exhibited a higher performance (30%) in comparison to the USY zeolite in the nitrobenzene conversion. Feijen et al. [28] reported that the EMT zeolite showed molecular shape selectivity in decane isomerization and heptadecane hydrocracking compared to the FAU zeolite. Gao et al. [29] found that the intergrowth of EMT and FAU zeolite resulted in an appropriate pore structure and suitable Brønsted and Lewis acidity, and thus

the CoMo catalyst supported on the EMT/FAU intergrowth zeolite, exhibited a good balance between hydrodesulfurization efficiency and research octane number.

Herein, the Pd-containing EMT zeolite catalyst (Pd/EMT) was prepared and used for the indirect oxidative carbonylation of methanol to dimethyl carbonate (DMC, $(CH_3O)_2CO$). The high activity, selectivity and stability of the Pd/EMT catalyst in comparison to conventional Pd/FAU catalyst for the indirect oxidative carbonylation of methanol to DMC are demonstrated.

2. Experimental

2.1. Catalyst preparation

The Na-form of EMT zeolite was synthesized according to the published procedure using a precursor mixture with the following molar composition: 1.0 SiO_2 : 0.1 Al_2O_3 : 0.24 Na_2O : 14.0 H_2O : 0.1 18-crown-6 [30]. The initial materials sodium aluminate (41 wt. % Al_2O_3, Sinopharm Chemical Reagent Co., Ltd., China), colloidal silica (Ludox-HS, 30 wt. % SiO_2, Aldrich), sodium hydroxide (NaOH, 96 wt. %, Xilong Scientific Co., Ltd., China) and 18-crown-6 (99 wt. %, Shanghai Macklin Biochemical Co., Ltd., China) were mixed in a polypropylene bottle and aged at room temperature (23 ºC) for 24 h. The aged mixture was transferred into a Teflon-lined autoclave and subjected to heating at 110 ºC for 15 days under static conditions. The crystalline product was filtered and thoroughly washed with deionized water. After drying at 80 ºC for 6 h, the samples were calcined at 550 ºC for 6 h in air to remove the crown ether template.

The Na-form FAU zeolite was synthesized from a precursor mixture with the following molar composition: 1.0 SiO_2 : 0.1 Al_2O_3 : 0.8 Na_2O : 40.0 H_2O. The initial materials aluminium hydroxide (Sinopharm Chemical Reagent Co., Ltd., China), colloidal silica (Ludox-HS, 30 wt. % SiO_2, Aldrich) and sodium hydroxide (NaOH, 96 wt. %, Xilong Scientific Co., Ltd., China) were mixed in a

polypropylene bottle and aged at room temperature (23 ºC) for 24 h. The aged mixture was transferred into a Teflon-lined autoclave and subjected to heating at 100 ºC for 12 h under static conditions. The crystalline product was filtered, washed and dried at 80 ºC for 6 h.

The introduction of palladium in both Na-form of EMT and FAU zeolites was performed according to the following procedure: palladium chloride ($PdCl_2$, 59.0 wt. % Pd, Sinopharm Chemical Reagent Co., Ltd., China) was dissolved in a dilute ammonia solution ($NH_3 \cdot H_2O$, 0.9 mmol L^{-1}) and then the resulting $Pd(NH_3)_4Cl_2$ solution was added dropwise into the as-prepared EMT or FAU zeolite slurry (liquid to solid mass ratio of 100). These mixtures were stirred (400 rpm) at 80 ºC for 6 h, and then the solid samples were separated by vacuum filtration and thoroughly washed with deionized water. After drying at 80 ºC for 6 h, the samples were calcined at 200 ºC for 2 h in air to obtain the Pd/EMT or Pd/FAU catalysts. The Pd content of the two catalysts (Pd/EMT and Pd/FAU) was 1.0 wt. %, if not specified.

2.2. Catalysts characterization

Transmission electron microscopy (TEM) study of the catalysts was performed on a JEOL JEM-2100 instrument. In addition, the scanning electron microscopy (SEM) characterization of the catalysts was performed on a JEOL JSM-7900F equipped with an energy dispersive X-ray spectrometer (EDS).

X-ray diffraction (XRD) patterns of the materials were collected on a Bruker D8 Advance diffractometer, using Cu Kα radiation. The chemical compositions of the samples were determined by inductively coupled plasma-atomic emission spectroscopy (ICP-AES) using a Thermo IRIS Intrepid II XSP. Additionally, X-ray photoelectron spectroscopy (XPS) characterization of samples was performed using an Escalab 250xi spectrometer with an Al Kα radiation (binding energy was referenced to the C 1s peak at 284.6 eV). N_2 physisorption (77 K) experiments were performed on a

Quantachrome Autosorb-IQ3 instrument. The specific surface area and pore size distribution were calculated using the Brunauer-Emmett-Teller (BET) theory and density functional theory (DFT) model based on the adsorption branch of the isotherms. Thermogravimetric-mass spectrometry (TG-MS) study was performed in a gas mixture of 20 vol. % O_2 and 80 vol. % N_2 on a Netzsch STA 449F5 instrument connected with QMS 403D mass spectrometer.

H_2-temperature programmed reduction (H_2-TPR) was carried out using a Tianjin Xianquan TP-5080 apparatus. The H_2 consumption was monitored by a thermal conductivity detector (TCD) or Tilon SR-D 200M mass spectrometer. Typically, 0.1000 g sample was pretreated in He flow (30 mL min^{-1}) at 200 ºC for 1 h and then cooled down to 20 ºC. Subsequently, a gas mixture of 10 vol. % H_2 in N_2 was introduced into the reactor. The H_2-TPR profiles were obtained in the range of 20–700 ºC with a heating rate of 10 ºC min^{-1} at a constant flow rate of 30 mL min^{-1}.

Diffuse reflectance infrared Fourier transform spectroscopy (DRIFTS) spectra of pyridine adsorption were measured on a Nicolet-6700 spectrometer. The sample was evacuated at 200 ºC for 5 h, followed by pyridine adsorption at room temperature (23 ºC) for 24 h and pyridine desorption in a vacuum at 150 ºC for 3 h. Subsequently, the spectra were recorded in absorption mode from 4000 cm^{-1} to 650 cm^{-1} at a resolution of 4 cm^{-1} over 64 scans.

DRIFTS experiments of CO adsorption were conducted on a Bruker Vertex 70 spectrometer equipped with a liquid N_2 cooling mercury-cadmium-telluride (MCT) detector and a Harrick Scientific HVC-DRP-4 reaction cell (ZnSe windows). The sample without diluents was placed into a reaction cell, prereduced in H_2 (30 mL min^{-1}) at 150 ºC for 1 h and flushed with N_2 (80 mL min^{-1}) at 200 ºC for 1 h. The sample was cooled down to 35 ºC for taking a background spectrum and subsequently, pure CO gas was introduced into the reaction cell at 30 mL min^{-1}. After 30 min adsorption, the sample

was flushed by N_2 flow (80 mL min^{-1}) at 35 ºC for 1 h and then the DRIFTS spectra were collected in the range of 35–200 ºC. Each spectrum was recorded in absorption mode from 4000 cm^{-1} to 600 cm^{-1} at a resolution of 4 cm^{-1} over 64 scans.

2.3. Catalytic tests

The schematic diagram of the apparatus used for the catalyst evaluation is shown in Scheme S2 (SI). The catalysts were tested in a fixed-bed quartz tubular microreactor (8 mm i.d. and 350 mm length) at 0.1 MPa. A K-type thermocouple was placed in the middle of catalyst bed for measuring the reaction temperature. The methyl nitrite (CH_3ONO) reactant was synthesized by dropping H_2SO_4 (9.3 mol L^{-1}) into an aqueous solution of CH_3OH and $NaNO_2$ ($2\ NaNO_2 + 2\ CH_3OH + H_2SO_4 \rightarrow 2\ CH_3ONO \uparrow + Na_2SO_4 + 2\ H_2O$), then collected into a steel cylinder and subsequently mixed with pure N_2 to obtain a gas mixture of CH_3ONO/N_2 (1/4, volume). Three calibrated mass flow controllers maintained the flow rates of pure N_2, gas mixtures of CO/N_2 (1/9, volume) and CH_3ONO/N_2. The gas mixture of $CO/CH_3ONO/N_2$ (1/6/33, volume) was fed into the microreactor, which was loaded with 0.1000 catalyst or 0.1000 g mixture of catalyst and α-Al_2O_3 (60–80 mesh). The catalyst of 0.0200 g was mixed with 1.9800 g α-Al_2O_3 (diluent) to obtain the mixture of catalyst and α-Al_2O_3. The reaction temperature was varied in the range of 100–120 ºC and the gas hourly space velocity (GHSV) was set at 8, 000 mL g^{-1} h^{-1} or 800, 000 mL g^{-1} h^{-1}. The on-line analysis was performed using a gas chromatography (GC; Agilent 7890B) equipped with thermal conductivity detector (TCD) connected to 5A and HayeSep Q packed columns (Agilent), and flame ionization detector (FID) connected to HP-Innowax capillary column (Agilent). The calculations of the turnover frequency (TOF), CO conversion, CH_3ONO conversion, DMC, dimethyl oxalate (DMO), methyl formate (MF) and dimethoxymethane (DMM) selectivity were shown in Supporting Information (SI).

3. Results and discussion

3.1. General properties of Pd/EMT and Pd/FAU catalysts

The size and morphology of both Pd/EMT and Pd/FAU catalysts were evaluated by SEM (Fig. 1). The typical hexagonal and cubic morphology for the EMT and FAU crystals are seen in the SEM images. The FAU crystals have a size of 2–4 μm while the EMT crystals have a size of 3–5 μm and a thickness of 0.5–0.8 μm. The high crystallinity of both samples is confirmed by XRD (Fig. 2) [31,32]. The EMT zeolite has three characteristic Bragg peaks in the range of 5–7 º 2Theta (Fig. 2a), which are indexed as (100), (002) and (101) reflections [31,33]. The most intense Bragg peak of (111) at 6.2 º 2Theta is present in the XRD pattern of FAU zeolite (Fig. 2b). The Pd/EMT and Pd/FAU catalysts exhibit similar XRD patterns thus indicating that the Pd loading had negligible effect on the crystallinity of both EMT and FAU zeolite supports (Fig. 2). No Bragg peaks ascribed to PdO (JCPDS 88-2434) and Pd^0 (JCPDS 87-0638) were detected for the Pd/EMT and Pd/FAU catalysts, possibly due to the high dispersion and low content. The N_2 adsorption isotherms of both Pd/EMT and Pd/FAU catalysts revealed the features for type Ⅰ Langmuir isotherm, typical of microporous materials (Fig. S1). Both Pd/EMT and Pd/FAU catalysts have almost the same BET surface area of 913–916 $m^2\ g^{-1}$ and micropore volume of 0.33 $cm^3\ g^{-1}$ (Table 1). The chemical compositions of the Pd/EMT and Pd/FAU catalysts were presented in Table 1. The Si/Al ratios for Pd/EMT and Pd/FAU catalysts are 4.2 and 2.2, respectively (Table 1). The difference in the chemical compositions of the two zeolites is due to the fact that the EMT zeolite was synthesized with an organic template while the FAU zeolite was prepared with sodium hydroxide; similar results have been reported previously [30,34,35]. The Pd/EMT catalyst showed lower Na content than the Pd/FAU catalyst (7.6 wt. % *vs.* 10.4 wt. %), as the result of higher Si/Al ratio of EMT zeolite. Both Pd/EMT and Pd/FAU catalysts contain the same

amount of Pd, i.e. 0.97–0.99 wt. % (Table 1).

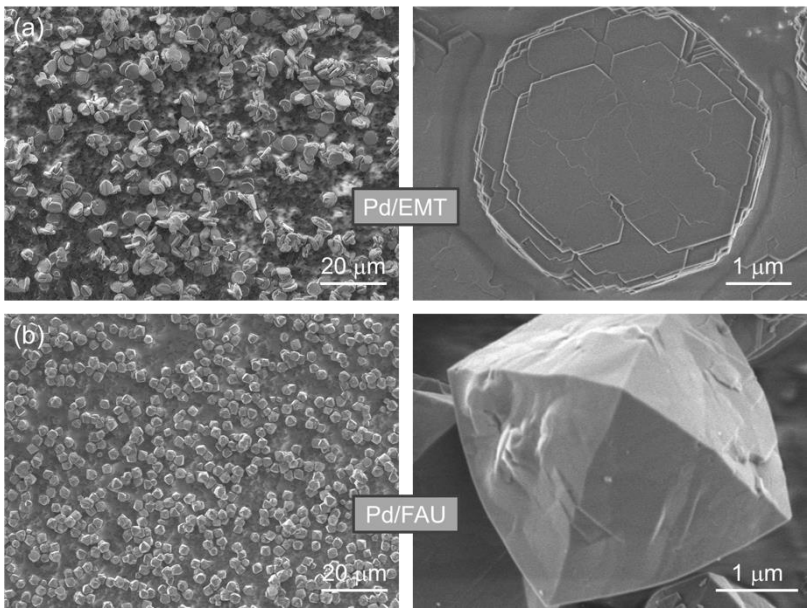

Fig. 1. SEM images of the (a) Pd/EMT and (b) Pd/FAU catalysts.

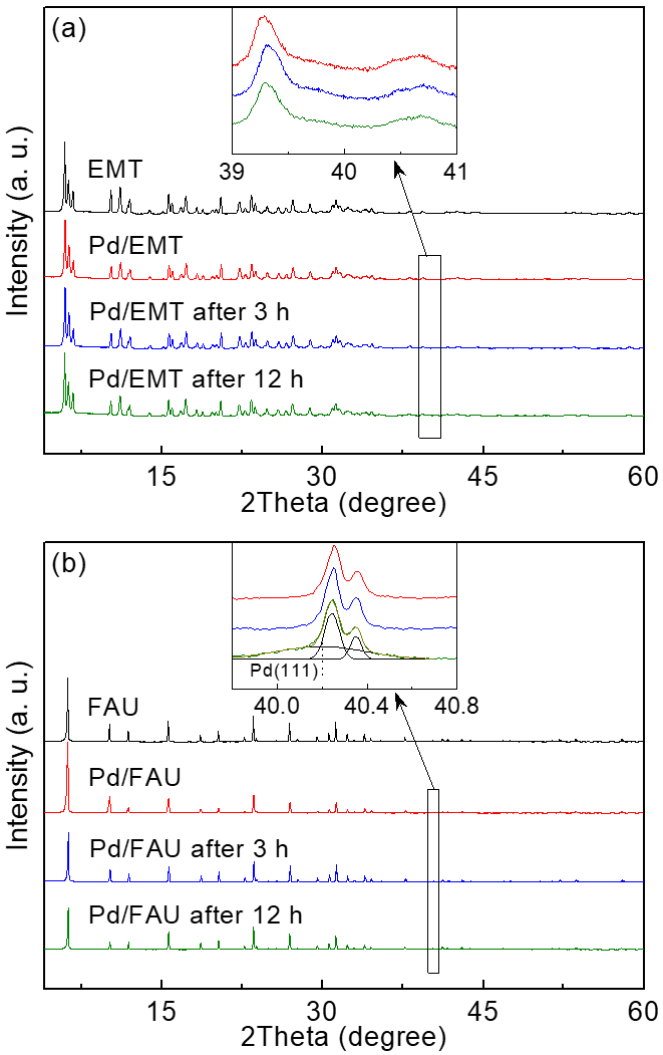

Fig. 2. (a) XRD patterns of EMT zeolite support, and Pd/EMT catalyst before and after catalytic tests (indirect oxidative carbonylation of methanol to DMC for 3 h and 12 h). (b) XRD patterns of FAU zeolite support, and Pd/FAU catalyst before and after catalytic tests for 3 h and 12 h. *Inset*: XRD patterns in the range of 39–41 º 2Theta and 39.8–40.8 º 2Theta. XRD pattern of Pd/FAU catalyst after 12 h test (39.8–40.8 º 2Theta) was deconvoluted using the Gaussian function. The peak at 40.2 º 2Theta with a full width at half-maximum (FWHM) of 0.41 was assigned to Pd(111).

Table 1 Physicochemical properties of the Pd/EMT and Pd/FAU catalysts and their catalytic performance in the indirect oxidative carbonylation of methanol to DMC.

Catalyst	S_{BET} ($m^2\ g^{-1}$)[a]	V_{micro} ($cm^3\ g^{-1}$)[a]	Si/Al ratio[b]	Pd (wt. %)[b]	Na (wt. %)[c]	TOF (s^{-1})[d]	E_a (kJ mol^{-1})[e]
Pd/EMT	913	0.33	4.2	0.99	7.6	0.25	72.7 ± 1.9
Pd/FAU	916	0.33	2.2	0.97	10.4	0.11	65.6 ± 1.6

[a] BET surface area, and the micropore volume determined by the *t*-plot method.

[b] Si/Al molar ratio and the Pd content determined by ICP-AES.

[c] The Na content measured by EDS elemental mapping (an average of at least 6 measurements).

[d] Measured according to the CO conversion and Pd atoms (details provided in SI). Reaction conditions: 0.1000 g mixture of catalyst and α-Al_2O_3 (diluent), $CO/CH_3ONO/N_2$ = 1/6/33 (volume), GHSV = 800, 000 mL g^{-1} h^{-1}, 110 ºC, 0.1 MPa. The catalyst of 0.0200 g was mixed with 1.9800 g α-Al_2O_3, and then 0.1000 g mixture of the catalyst and α-Al_2O_3 was used for the catalyst testing.

[e] Apparent activation energy calculated from the Arrhenius plots in Fig. 4 (details provided in SI).

3.2. Pd/EMT and Pd/FAU catalysts in indirect oxidative carbonylation of methanol to dimethyl carbonate

The catalytic activity of both Pd/EMT and Pd/FAU catalysts in the indirect oxidative carbonylation of methanol to DMC as a function of time on stream is presented in Fig. 3. The Pd/EMT catalyst showed stable conversion and selectivity within 12 h (Fig. 3a), while the CO conversion decreased from 89% to 21% on the Pd/FAU catalyst (Fig. 3b). Both CO and CH_3ONO conversions decreased remarkably within 12 h over the Pd/FAU catalyst, indicating the rapid deactivation (Fig. 3b). The selectivity of main product DMC was increased significantly from 56% to 87% within the first 6 h on the Pd/FAU catalyst, possibly due to the decrease of byproduct selectivity of dimethoxymethane (DMM) from 33% to 6%. Beyond 6 h reaction, the selectivity of the methyl formate (MF) and dimethyl

oxalate (DMO) byproducts increased gradually while the DMC selectivity decayed (Fig. 3b). The appearance of DMO and obvious increase of MF likely suggested the generation of large Pd particles, since Pd particles are considered to be the active sites for the formation of DMO and MF byproducts [36,37]. Consequently, the deactivation behavior of the Pd/FAU catalyst was initially attributed to the sintering of Pd. It should be noted that no DMO byproduct was detected on the Pd/EMT catalyst within 12 h catalytic test (Fig. 3a).

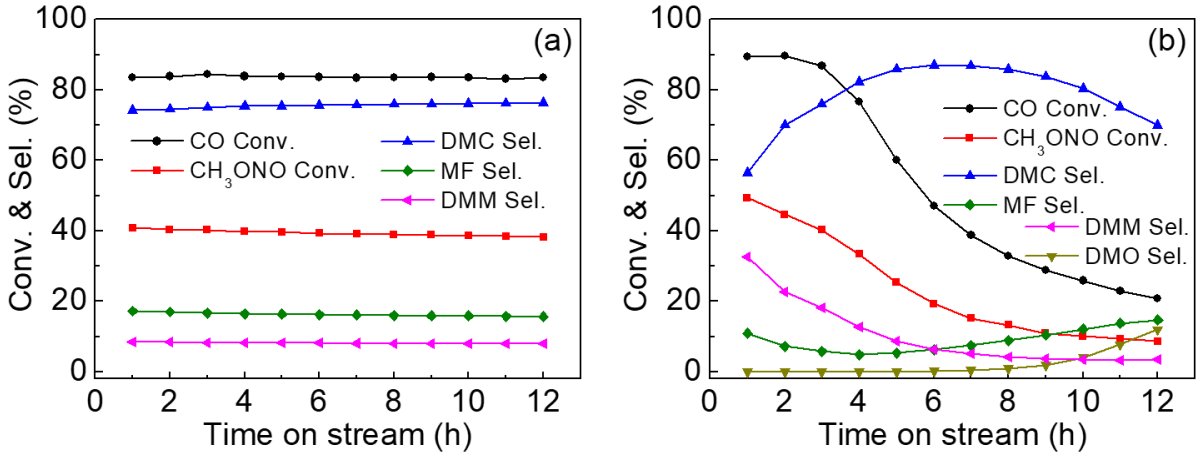

Fig. 3. Conversion of CO and methyl nitrite (CH_3ONO), and selectivity of dimethyl carbonate (DMC), methyl formate (MF), dimethoxymethane (DMM) and dimethyl oxalate (DMO) as a function of time in the indirect oxidative carbonylation of methanol to DMC on catalysts (a) Pd/EMT and (b) Pd/FAU. Reaction conditions: 0.1000 g catalyst, $CO/CH_3ONO/N_2$ = 1/6/33 (volume), GHSV = 8, 000 mL g^{-1} h^{-1}, 110 ºC, 0.1 MPa. For each point an average of 3 measurements was conducted.

The apparent activation energies and TOF values for the indirect oxidative carbonylation of methanol to DMC were calculated and shown in Table 1 and Fig. 4 (details provided in SI). The Pd/EMT and Pd/FAU catalysts showed similar apparent activation energies of 72.7 ± 1.9 kJ mol^{-1} and 65.6 ± 1.6 kJ mol^{-1}, respectively under the identical reaction conditions (Fig. 4). This suggested that the reaction pathway and/or the rate-determining step were equivalent on the two catalysts [37,38].

However, the Pd/EMT catalyst showed a TOF (namely, intrinsic activity) of 0.25 s^{-1}, larger than that of 0.11 s^{-1} for the Pd/FAU catalyst (Table 1). The improved intrinsic activity was possibly assigned to the different properties of EMT and FAU zeolite framework.

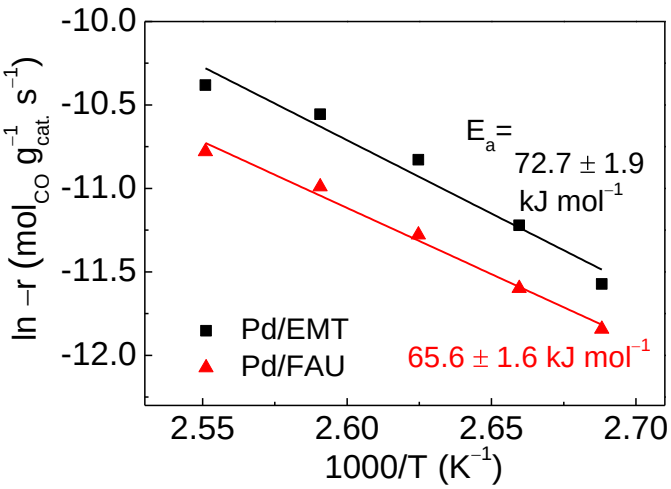

Fig. 4. Arrhenius plot for the indirect oxidative carbonylation of methanol to DMC over the Pd/EMT and Pd/FAU catalysts (E_a, apparent activation energy). Reaction conditions: 0.1000 g mixture of catalyst and α-Al_2O_3 (diluent), $CO/CH_3ONO/N_2$ = 1/6/33 (volume), GHSV = 800, 000 mL g^{-1} h^{-1}, 0.1 MPa. The kinetic data were acquired within the differential regime while the CO conversion was controlled below 13% (details provided in SI). The catalyst of 0.0200 g was mixed with 1.9800 g α-Al_2O_3, and then 0.1000 g mixture of the catalyst and α-Al_2O_3 was used for the catalyst testing.

3.3. Features of stable Pd/EMT and deactivated Pd/FAU catalysts

The Pd/EMT and Pd/FAU catalysts after 12 h catalytic test of the indirect oxidative carbonylation of methanol to DMC were characterized by TG-MS analysis; the results are depicted in Fig. 5. The weight loss measured for the used Pd/EMT and Pd/FAU catalysts occurred in two stages (Fig. 5). The first stage is in the range of 35–170 ºC and corresponds to the removal of physically adsorbed water, which is evidenced by the MS curves [39,40]. In the second stage (170–280 ºC), a single peak at 226

ºC for the Pd/EMT catalyst and two peaks at 179 ºC and 220 ºC for the Pd/FAU catalyst were measured. The DTG results are consistent with the MS, which is revealing the desorption of abundant amount of water as well as carbon dioxide at the same temperatures. The second stage is assigned to the loss of water strongly bound to the zeolite framework and to the thermal decomposition of residual reaction species such as $(CH_3O)_2CO$ and CH_3OCO [40,41]. Based on the peak area of the CO_2 formation (170–280 ºC), the amount of the residual reaction species on the used Pd/EMT and Pd/FAU catalysts was estimated to be 0.032 g $g_{cat.}^{-1}$ and 0.036 g $g_{cat.}^{-1}$, respectively. No oxidation peaks of CO_2 formation were found above 300 ºC (see TG-DTG and MS results), which suggested that the carbon deposits were not detectable on both Pd/EMT and Pd/FAU catalysts [42,43]. These results confirmed that the deactivation behavior of Pd/FAU catalyst cannot be attributed to the residual reaction species or carbon deposits.

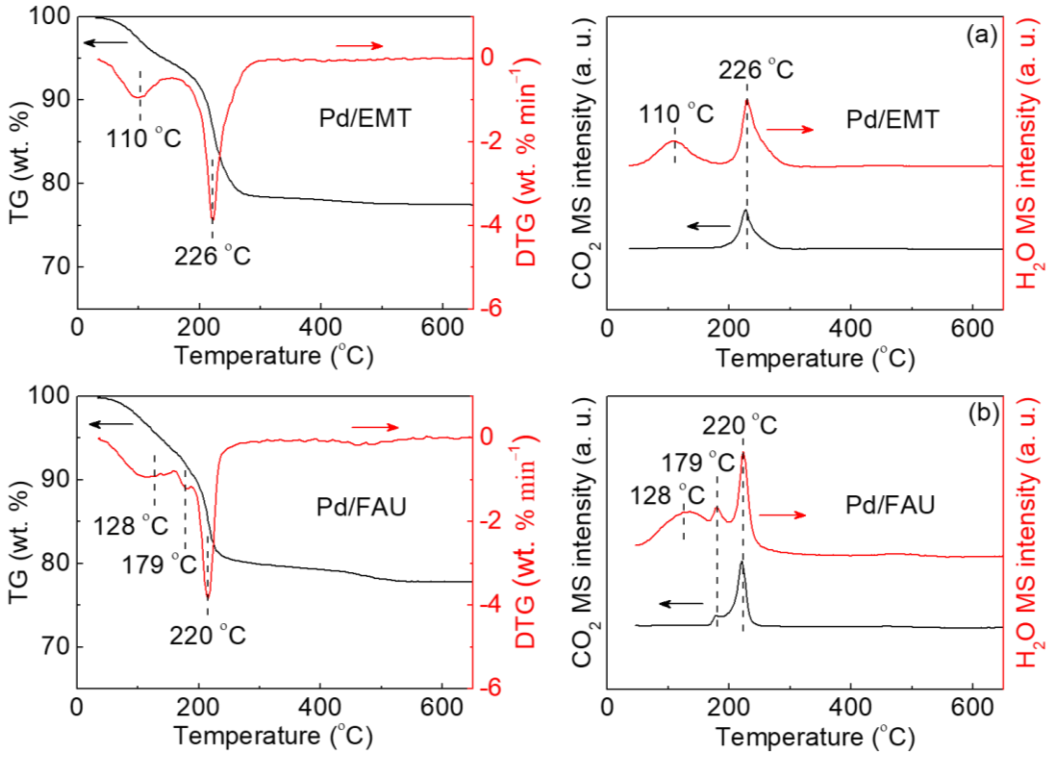

Fig. 5. TG-DTG (left) and MS (right) curves of the (a) Pd/EMT and (b) Pd/FAU catalysts after 12 h catalytic test (indirect oxidative carbonylation of methanol to DMC).

The DRIFTS spectra for both Pd/EMT and Pd/FAU catalysts using pyridine are presented in Fig. 6. The bands at 1442 cm^{-1} (pyridine coordinated to Na^+ ions), 1457 cm^{-1} (pyridine interacting with coordinately unsaturated Al^{3+} ions), 1574 cm^{-1} (weak Lewis acidity), 1593 cm^{-1} (hydrogen-bound pyridine) and 1611 cm^{-1} (hydrogen-bound pyridine) are assigned to Lewis-bound pyridine; the bands at 1542 cm^{-1} and 1637 cm^{-1} are attributed to Brønsted-bound pyridine, and the band at 1487 cm^{-1} is assigned to pyridine associated with both Lewis and Brønsted acid sites [44–47]. Brønsted acid sites on both Pd/EMT and Pd/FAU catalysts possibly resulted from the ion exchange between Na^+ and NH_4^+ (dissociation of $NH_3{\cdot}H_2O$) during the preparation of catalysts, since the Na-form of EMT and FAU zeolites should be in the absence of Brønsted acidity [45,48]. Brønsted acid sites could lead to the formation of methyl formate byproduct during the indirect oxidative carbonylation of methanol to DMC [18,49]. Using the band areas at 1542 cm^{-1} and 1442 cm^{-1}, the amount of Brønsted and Lewis acid sites was estimated, respectively (Fig. 6 and Table S1). Brønsted acid sites of 5.1 area mg^{-1} for the Pd/FAU catalyst were lower than 8.5 area mg^{-1} for the Pd/EMT catalyst after the catalytic test (Table S1). This is consistent with the catalytic results showing lower selectivity towards methyl formate (MF) byproduct with the Pd/FAU catalyst than with the Pd/EMT catalyst (Fig. 3). However, the Pd/EMT catalyst showed higher Lewis acid sites than the Pd/FAU catalyst after the catalytic test (47.4 area mg^{-1} *vs.* 38.1 area mg^{-1}, Table S1). This possibly contributed to the stable activity of the Pd/EMT catalyst (Fig. 3), because Lewis acid sites could accept electrons from the Pd species and thus promote the formation of the Pd^{2+} active sites as previously stated [18].

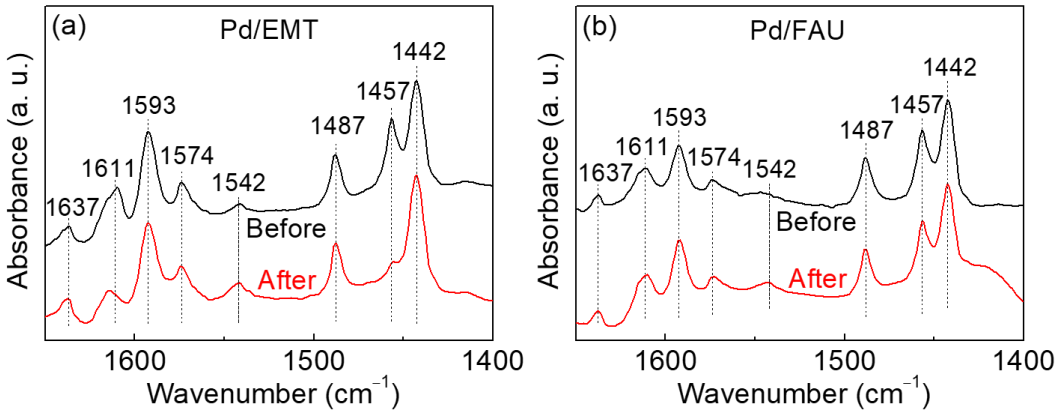

Fig. 6. DRIFTS spectra of pyridine adsorbed on (a) Pd/EMT and (b) Pd/FAU catalysts before and after catalytic test (indirect oxidative carbonylation of methanol to DMC for 12 h).

TEM study of the Pd/EMT and Pd/FAU catalysts was performed to determine the size and distribution of palladium. As shown in Fig. 7a–d, both fresh and used Pd/EMT catalysts showed the characteristic hexagonal platelike morphology and the crystalline fringes associated with EMT zeolite [50]. As described previously, the Pd/EMT and Pd/FAU catalysts were prepared by ion exchange (Pd precursor: $Pd(NH_3)_4^{2+}$), and the ion-exchanged samples were calcined at 200 ºC. The TG-MS results suggested that the low-temperature calcination of the catalysts (200 ºC) caused the $Pd(NH_3)_4^{2+}$ to lose partially the NH_3 ligand and to generate the $Pd(NH_3)_x^{2+}$ ($x < 2$) sites that are anchored on the zeolite framework (Fig. S2) [51,52]. Neither Pd clusters nor nanoparticles were visible in the TEM images of fresh Pd/EMT and Pd/FAU catalysts (Fig. 7b,f). In contrast, mono-dispersed Pd clusters (< 1 nm) confined within the used Pd/EMT catalyst after 12 h catalytic test could be observed (Fig. 7d and Fig. S3). In comparison to the fresh Pd/FAU catalyst, the used catalyst contained large Pd nanoparticles located predominantly on the external surface of the FAU crystals (Fig. 7e,g). The presence of Pd nanoparticles was also identified by SEM and further confirmed by the EDS (Fig. S4). The aggregated Pd formed large nanoparticles with random distribution, i.e. 2.4 or 10.6 wt. % on the surface of the

used Pd/FAU catalyst (Fig. 8), whereas the uniform Pd distribution on the used Pd/EMT catalyst (1.9 or 2.1 wt. %) is confirmed by EDS elemental mapping (Fig. 8). Furthermore, TEM revealed the Pd sintering with different particle sizes ranging from 3 nm to 25 nm deposited on the external surface and the edges of used Pd/FAU catalyst (Fig. 7h). The average size of the Pd nanoparticles on the Pd/FAU catalyst was estimated to be 8.7 nm based on measuring 200 nanoparticles (*inset* of Fig. 7h). This finding is consistent with the catalytic results showing a remarkable increase of the DMO and MF byproducts beyond 6 h catalytic test (Fig. 3b). The large Pd nanoparticles have been shown to be the active sites for the formation of DMO and MF byproducts earlier [36,37].

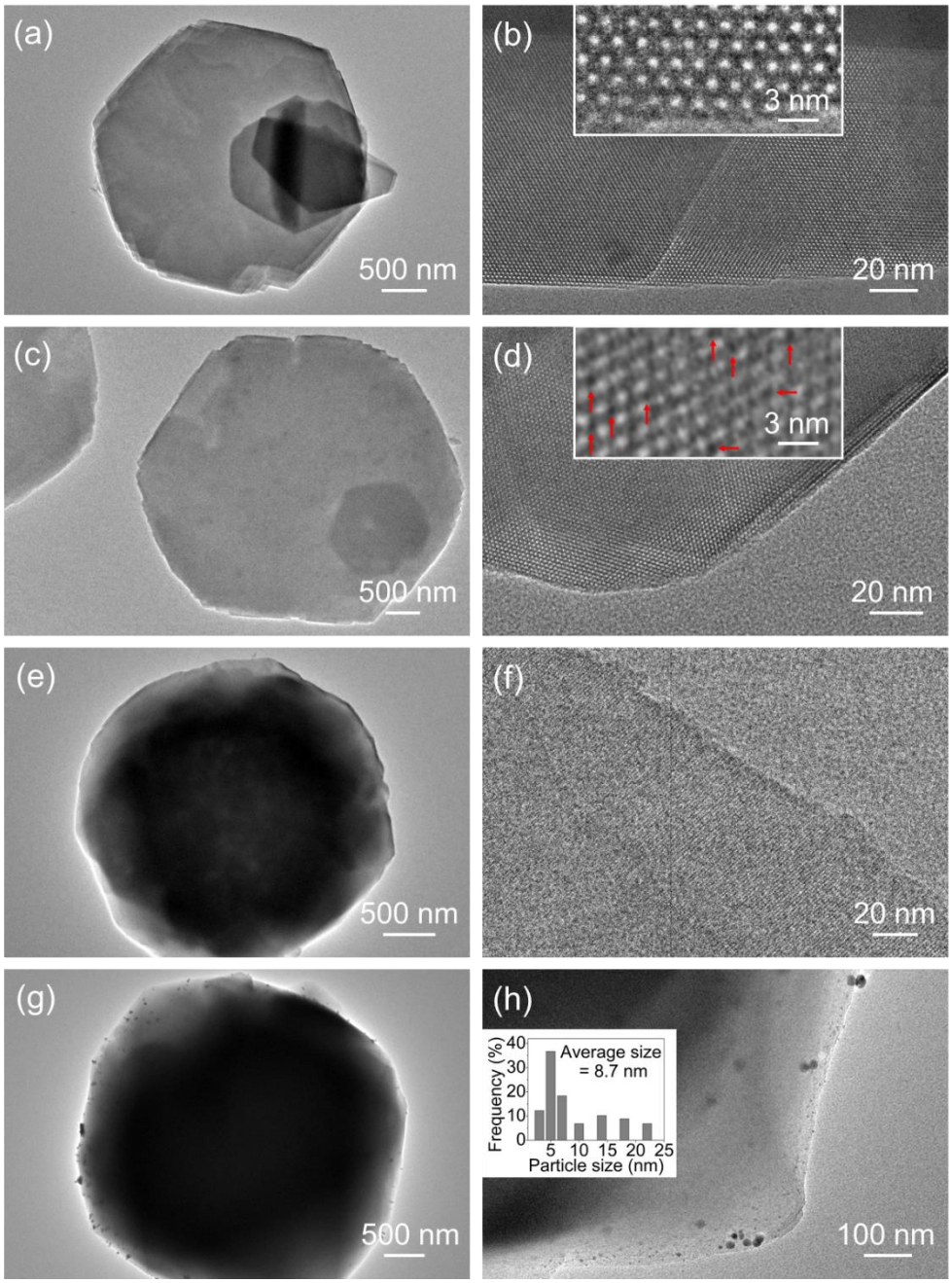

Fig. 7. TEM images of (a,b) fresh and (c,d) used Pd/EMT catalysts after 12 h catalytic test (b,d, *inset*: enlarged area); TEM images of (e,f) fresh and (g,h) used Pd/FAU catalysts after 12 h catalytic test (h, *inset*: Pd particle size distribution estimated based on measuring 200 nanoparticles).

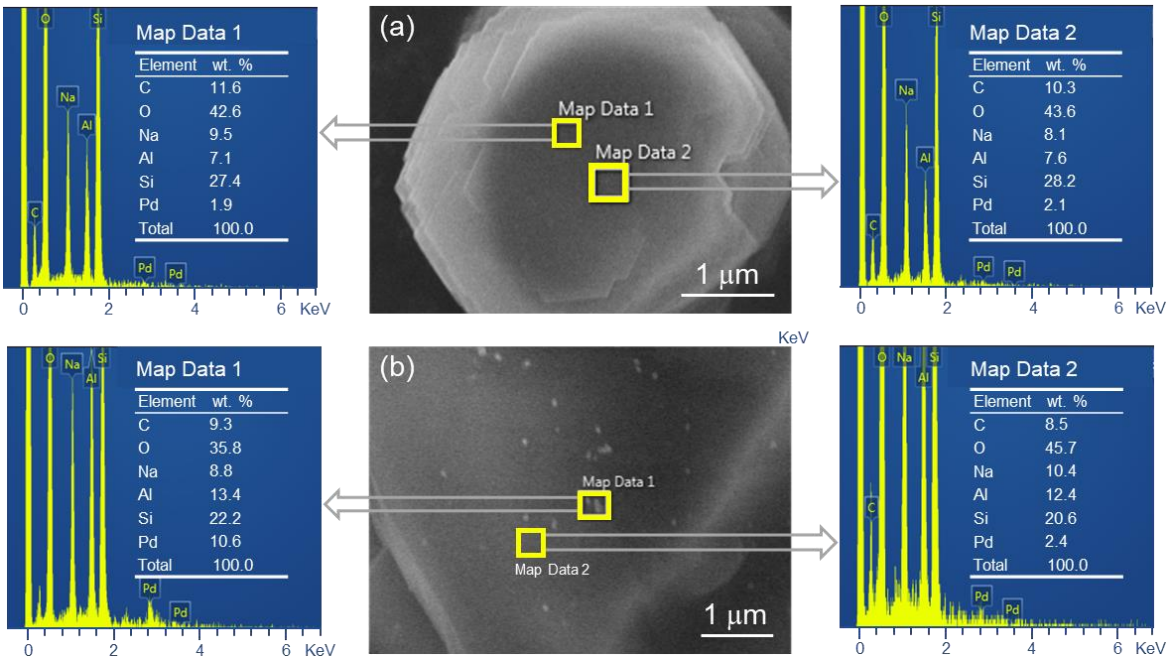

Fig. 8. SEM images and EDS elemental mapping of used (a) Pd/EMT and (b) Pd/FAU catalysts after 12 h catalytic test. The Pd content in different regions of the Pd/EMT catalyst is similar (1.9 wt. % or 2.1 wt. %), while the Pd content in the Pd/FAU catalyst is varied (2.4 wt. % or 10.6 wt. %).

In the case of Pd/EMT catalyst after 3 h and 12 h catalytic test, no Bragg peaks corresponding to PdO (JCPDS 88-2434) and Pd^0 (JCPDS 87-0638) were observed (Fig. 2a). The Bragg peak of Pd(111) is overlapped with that of FAU zeolite in the range of 39.8–40.8 º 2Theta. After the deconvolution, the peak of Pd(111) at 40.2 º 2Theta was clearly observed on the Pd/FAU catalyst after 12 h catalytic test (*inset* of Fig. 2b) indicating the Pd sintering. The size of Pd nanoparticles was 25 nm according to the calculation using the Scherrer-Debye equation; this size is larger than that of determined by TEM 8.7 nm (*inset* of Fig. 7h). Both TEM and XRD results demonstrated that palladium sintering occurred on the used Pd/FAU catalyst after 12 h catalytic test while no changes were observed on the used Pd/EMT catalyst.

As previously stated, the Pd^{2+} species is the active sites for the formation of DMC [10,15].

Therefore, the state of Pd in the used Pd/EMT and Pd/FAU catalysts was measured by XPS. As shown in Fig. 9a, the peaks at 336.3 eV and 341.6 eV were attributed to the Pd^0 species while the peaks at 338.3 eV and 343.5 eV indicated the presence of Pd^{2+} species [53,54]. These binding energies were 0.8–1.3 eV higher than the counterparts of conventional Pd^0 and Pd^{2+} species due to Lewis acid sites of the Pd/EMT catalyst [18,37,55]. Lewis acid sites are considered to be electron acceptors and thus made the Pd species lose the electrons [18]. The Pd^{2+} species may result from Pd clusters/nanoparticles charged by the zeolite framework through the formation of Pd-O ionic bonds [10,19]. Moreover, Pd^{2+} species also could be generated during the synthesis of DMC, since the reaction follows a mechanistic pathway of oxidative addition and reductive elimination, and the Pd active sites undergo the $Pd^0 \rightarrow Pd^{2+} \rightarrow Pd^0$ pathway [10,16]. As shown in Fig. 9b, the Pd/FAU catalyst exhibited four peaks corresponding to Pd^0 and Pd^{2+} species, being lower by 0.5–0.7 eV in comparison to the Pd/EMT catalyst. This was attributed to the different properties of EMT and FAU zeolite framework. As shown by XPS, the peak area ratio of $Pd^{2+}/(Pd^{2+}+Pd^0)$ for the Pd/FAU catalyst decreased remarkably from 79% to 36% with increasing the reaction time from 3 h to 12 h (Table 2). In contrast, the peak area ratio of $Pd^{2+}/(Pd^{2+}+Pd^0)$ for the Pd/EMT catalyst declined from 69% to 54% (Table 2).

In order to oxidize Pd^0 into Pd^{2+} species in the used Pd/FAU catalyst after 12 h catalytic test, a subsequent calcination was carried out at 200 ºC for 2 h in air. After this calcination, the CO conversion was increased substantially from 21% to 76% (Fig. S5). However, with prolonged reaction time, the Pd^{2+} species was gradually reduced by CO reactant, and the Pd/FAU catalyst showed similar deactivation behavior to the fresh catalyst (Fig. 3b and Fig. S5). The combined TEM and XPS results indicate that the palladium sintering and reduction of Pd^{2+} to Pd^0 cause the deactivation of Pd/FAU catalyst.

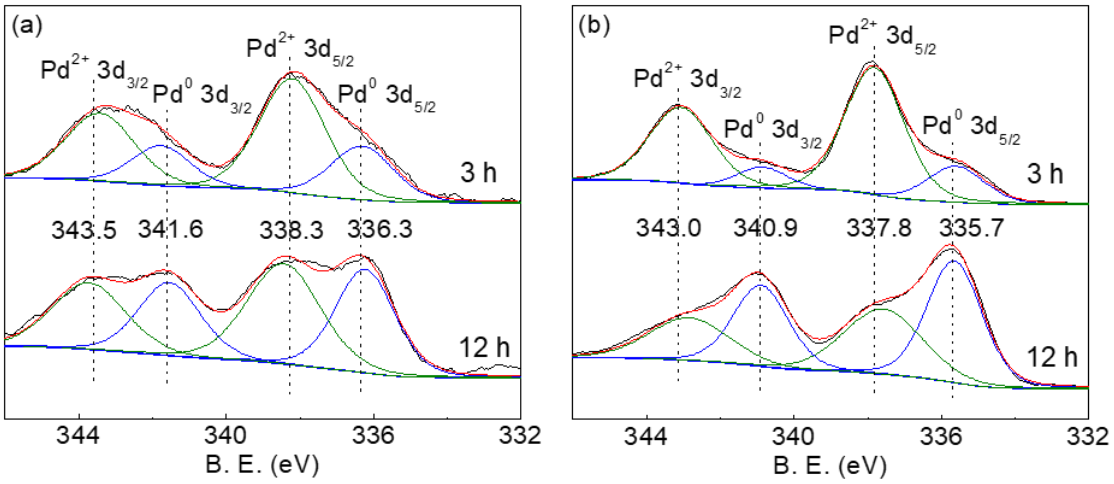

Fig. 9. XPS spectra of the used (a) Pd/EMT and (b) Pd/FAU catalysts after 3 h and 12 h catalytic test.

Table 2 Peak areas of Pd^{2+} and Pd^{0}, and the $Pd^{2+}/(Pd^{2+}+Pd^{0})$ area ratio determined by XPS.[a]

Catalyst	Reaction time (h)	Area of Pd^{2+}	Area of Pd^{0}	Area ratio of $Pd^{2+}/(Pd^{2+}+Pd^{0})$
Pd/EMT	3	11067[b]	4920[b]	69%
	12	10518[b]	8800[b]	54%
Pd/FAU	3	11077[c]	2986[c]	79%
	12	5974[c]	10477[c]	36%

[a] XPS spectra of used Pd/EMT and Pd/FAU catalysts after 3 h and 12 h catalytic test (Fig. 9).

[b] Peak areas of Pd^{2+} at 338.3 eV and Pd^{0} at 336.3 eV based on XPS spectra of Pd/EMT catalysts.

[c] Peak areas of Pd^{2+} at 337.8 eV and Pd^{0} at 335.7 eV based on XPS spectra of Pd/FAU catalysts.

3.4. Stabilization of Pd in EMT and FAU zeolites

Carbon monoxide is a probe molecule widely employed to elucidate the nature of electron donor Pd species. The DRIFTS spectra of CO adsorbed on the reduced Pd/EMT and Pd/FAU catalysts in the range of 35–200 ºC are presented in Fig. 10. For the Pd/EMT catalyst after 3 h catalytic test (Fig. 10a),

the band at 2135 cm^{-1} is attributed to linear CO interacting with Pd^{2+} species; the bands at 2094 cm^{-1} and 2052 cm^{-1} are assigned to linear CO adsorbed on Pd^0 species; and the bands at 1977 cm^{-1} and 1906 cm^{-1} are associated with bridged CO adsorbed on Pd^0 species [41,56]. Both bands corresponding to linear and bridged CO were progressively decreased with increasing the temperature from 35 ºC to 100 ºC, and disappeared at 150 ºC (Fig. 10a). The DRIFTS spectra of Pd/EMT catalyst after 3 h and 12 h catalytic test are almost identical in the whole temperature range of 35–200 ºC (Fig. 10a,b) indicating the stability of the Pd species on the Pd/EMT catalyst. This result is in accordance with the stable catalytic performance of the Pd/EMT catalyst (Fig. 3a). As shown in Fig. 10b, linear CO (2135 cm^{-1}, 2086 cm^{-1}, 2029 cm^{-1} and 2034 cm^{-1}) and bridged CO (1894 cm^{-1} and 1854 cm^{-1}) were identified on the Pd/FAU catalysts after 3 h and 12 h catalytic test. Compared to the Pd/EMT catalysts, the bands of bridged CO on the Pd/FAU catalysts were clearly increased (Fig. 10), which is possibly due to the sintering of Pd [57,58]. The Pd/EMT catalysts exhibited a clear blue shift of both linear and bridged CO bands compared to the Pd/FAU catalysts (2086 < 2094, 2029 and 2034 < 2052, 1894 < 1977, 1854 < 1906 cm^{-1}; see Fig. 10). This suggested the π back-donation was weak and thus the Pd-CO bond was weakened on the Pd/EMT catalyst [59,60]. This infers that the interactions between Pd and the EMT zeolite framework were stronger than within the FAU zeolite framework. As reported previously [24,25], the difference in the topology of EMT and FAU zeolites leads to the different locations of cations: Ⅰ, Ⅰ’ and Ⅱ in the FAU *vs.* $Ⅰ_a$, $Ⅰ_b$, $Ⅰ'_a$, $Ⅰ'_b$, $Ⅱ_a$ and $Ⅱ_b$ in the EMT (Fig. S6). These different cation locations have a significant influence on the interactions between metal clusters and zeolites [25,61,62]. Therefore, the stabilization of mono-dispersed Pd clusters within the EMT zeolite was attributed to the enhanced interactions between Pd and EMT zeolite, as the result of the suitable negative charge distribution, abundant Lewis acid sites (Table S1) and unique cage

structure, i.e. hypocage and hypercage for EMT *vs.* supercage for FAU [31,63,64].

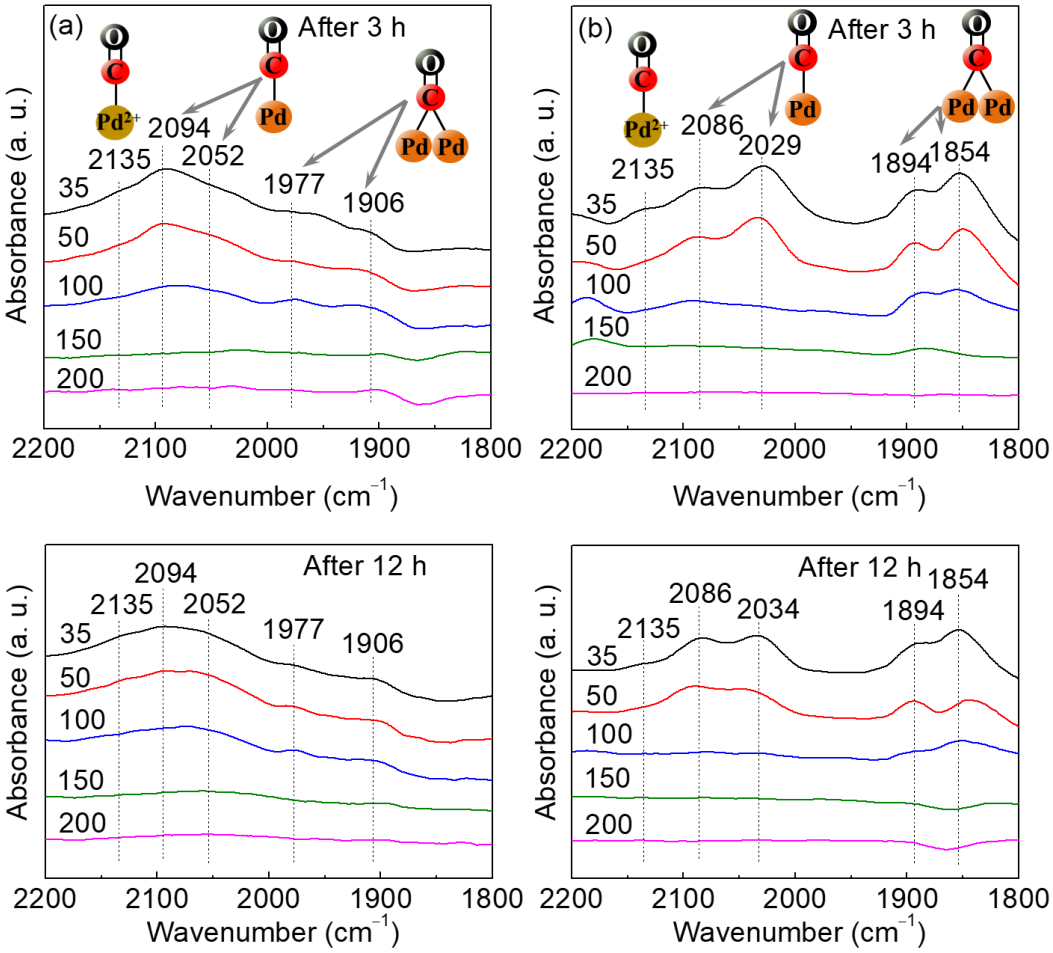

Fig. 10. DRIFTS spectra of CO adsorbed on (a) Pd/EMT and (b) Pd/FAU catalysts after 3 h and 12 h catalytic test at different temperatures: 35 ºC, 50 ºC, 100 ºC, 150 ºC and 200 ºC. The samples were prereduced in H_2 at 150 ºC, purged in N_2 at 200 ºC, cooled down to 35 ºC, exposed to excess of CO and then flushed by N_2; the spectra were recorded in the range of 35–200 ºC.

To further understand the interactions between Pd and zeolite framework, H_2-temperature programmed reduction (H_2-TPR) experiments were conducted on both Pd/EMT and Pd/FAU catalysts. The H_2-TPR profiles of the two catalysts contain low- and high-temperature reduction peaks, which were assigned to the weak- and strong-interaction Pd species with zeolite framework, respectively (Fig. 11) [51,65,66]. Similar low- and high-temperature reduction peaks were also measured by mass

spectrometer for a new Pd/EMT catalyst loaded with 5 wt. % Pd (Fig. S7). A negative peak (H_2 desorption) below 100 ºC, usually assigned to the decomposition of Pd β-hydride, was not detected for Pd/EMT or Pd/FAU catalysts (Fig. 11). This result suggests that Pd was highly dispersed on the both fresh Pd/EMT and Pd/FAU catalysts [67,68]. About 82% of Pd^{2+} in the EMT zeolite (Pd/EMT catalyst) was difficult to be reduced due to the enhanced metal-support interactions, while only 37% of Pd^{2+} in the FAU zeolite was difficult (Pd/FAU catalyst) (Fig. 11). This indicates that the interactions between Pd and zeolite framework in the Pd/EMT catalyst were much stronger than that in the Pd/FAU catalyst. The enhanced interactions between Pd and EMT zeolite framework stabilized the Pd/EMT catalyst as shown by DRIFTS and H_2-TPR results.

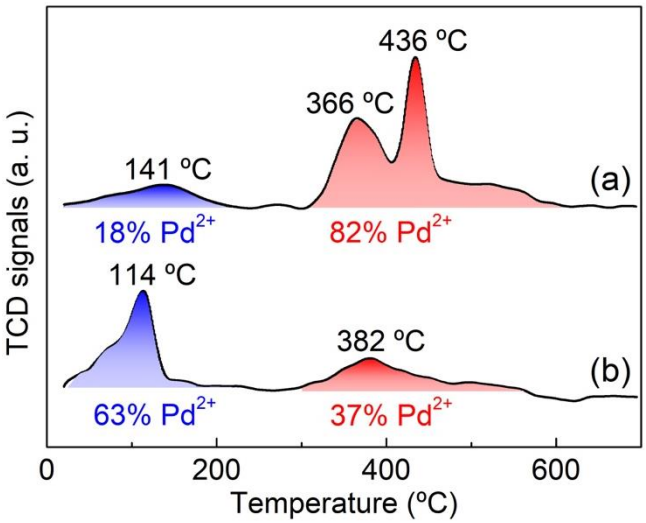

Fig. 11. H_2-TPR profiles of fresh (a) Pd/EMT and (b) Pd/FAU catalysts; the peak area ratios of low- and high-temperature peaks to the sum of low- and high-temperature peaks are presented in percentages.

3.5. Stability of Pd/EMT catalyst

As previously stated, the stability of the catalysts for the indirect oxidative carbonylation of

methanol to DMC is always a big challenge, especially when they are used in real reaction conditions [11,19]. A long-term catalytic test over the Pd/EMT catalyst was performed and the results are shown in Fig. 12. The conversion and selectivity of the Pd/EMT catalyst remain constant for at least 130 h test, i.e., CO conversion of 82 ± 1%, CH_3ONO conversion of 36 ± 2%, and DMC selectivity of 79 ± 2%. No DMO byproduct was detected over the Pd/EMT catalyst during the 130 h test. None of Bragg peaks corresponding to Pd^0 (JCPDS 87-0638) and PdO (JCPDS 88-2434) were observed for the used Pd/EMT catalyst after 130 h reaction (Fig. S8), indicating the excellent resistance to Pd sintering. The TEM study showed the uniform Pd clusters (about 1 nm) confined within the used Pd/EMT catalyst after 130 h reaction; the size and distrubution of the Pd clusters were the same as in the catalyst after 12 h catalytic test (Fig. 7d and Fig. S9). Moreover, in comparison with the catalysts reported in the literature, the Pd/EMT catalyst provided good activity and better stability (Table S2).

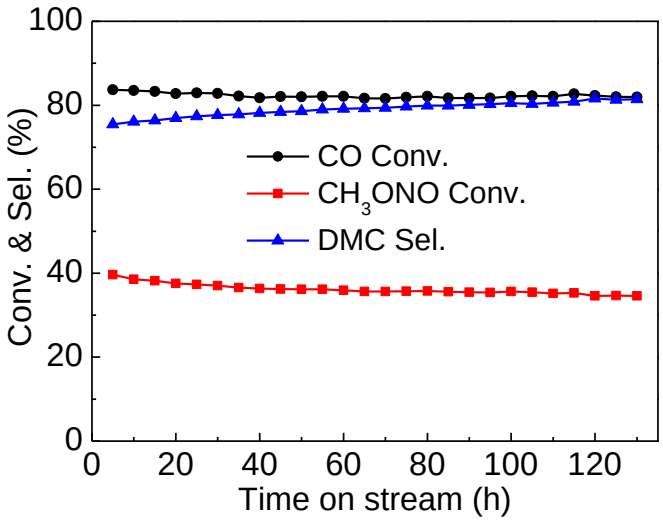

Fig. 12. Durability performance of the Pd/EMT catalyst in the indirect oxidative carbonylation of methanol to DMC measured for 130 h. Reaction conditions: 0.1000 g catalyst, $CO/CH_3ONO/N_2$ = 1/6/33 (volume), GHSV = 8, 000 mL g^{-1} h^{-1}, 110 °C, 0.1 MPa. For each point an average of 3 measurements was conducted.

4. Conclusions

The EMT zeolite was found to be a promising support for the stabilization of palladium clusters and preparation of Pd/EMT catalyst for the indirect oxidative carbonylation of methanol to dimethyl carbonate (DMC). The Pd/EMT catalyst exhibited higher intrinsic activity (i.e., turnover frequency) than conventional Pd/FAU catalyst. The conventional Pd/FAU catalyst was deactivated within 12 h due to the palladium sintering and decrease of Pd^{2+} active sites. In contrast, the Pd/EMT catalyst (1.0 wt. % Pd) showed high CO conversion of 82% and DMC selectivity of 79%, and good stability during the continuous test of 130 h. It was found that the catalyst stability is strongly dependent on the interactions between the Pd and zeolite framework. The enhanced interactions between Pd and EMT zeolite inhibited the sintering of palladium clusters and maintained the Pd^{2+} active sites in the catalyst. This work presents a newly designed Pd/EMT catalyst with great performance in the indirect oxidative carbonylation of methanol to DMC by understanding the benefit of the zeolite framework (EMT-type zeolite).

Declaration of Competing Interest

The authors declare that they have no known competing financial interests or personal relationships that could have appeared to influence the work reported in this paper.

Acknowledgements

This work was supported by the Natural Science Foundation of China (21908246, 21975285 , U1862118), China Postdoctoral Science Foundation (2017M622311), Fundamental Research Funds for the Central Universities (18CX02148A) and the Sino-French International Laboratory (LIA) “Zeolites”.

References

[1] S. Huang, B. Yan, S. Wang, X. Ma, Chem. Soc. Rev. 44 (2015) 3079−3116.

[2] A.A. Marciniak, O.C. Alves, L.G. Appel, C.J.A. Mota, J. Catal. 371 (2019) 88−95.

[3] G. Fiorani, A. Perosa, M. Selva, Green Chem. 20 (2018) 288−322.

[4] R. Saada, O. AboElazayem, S. Kellici, T. Heil, D. Morgan, G.I. Lampronti, B. Saha, Appl. Catal. B 226 (2018) 451−462.

[5] V. Crocellà, T. Tabanelli, J.G. Vitillo, D. Costenaro, C. Bisio, F. Cavani, S. Bordiga, Appl. Catal. B 211 (2017) 323−336.

[6] K. Xuan, Y. Pu, F. Li, J. Luo, N. Zhao, F. Xiao, Chin. J. Catal. 40 (2019) 553−566.

[7] X. Wang, R. Wang, X. Gu, J. Jia, Z. Zheng, Catal. Sci. Technol. 9 (2019) 1774–1778.

[8] Y. Liao, L. Feng, D. Xin, Z. Ning, F. Xiao, Chin. J. Catal. 38 (2017) 1860−1869.

[9] C.M. Marin, L. Li, A. Bhalkikar, J.E. Doyle, X.C. Zeng, C.L. Cheung, J. Catal. 340 (2016) 295−301.

[10] H. Tan, Z. Chen, Z. Xu, J. Sun, Z. Wang, R. Si, W. Zhuang, G. Guo, ACS Catal. 9 (2019) 3595−3603.

[11] H. Tan, Z. Wang, Z. Xu, J. Sun, Y. Xu, Q. Chen, Y. Chen, G. Guo, Catal. Today 316 (2018) 2−12.

[12] Y. Dong, Y. Shen, Y. Zhao, S. Wang, X. Ma, ChemCatChem 7 (2015) 2460−2466.

[13] S. Uchiumi, K. Ataka, T. Matsuzaki, J. Organomet. Chem. 576 (1999) 279−289.

[14] N. Keller, G. Rebmann, V. Keller, J. Mol. Catal. A: Chem. 317 (2010) 1−18.

[15] Y. Yamamoto, Catal. Surv. Asia 14 (2010) 103−110.

[16] H. Tan, Z. Wang, Z. Xu, J. Sun, Z. Chen, Q. Chen, Y. Chen, G. Guo, Catal. Sci. Technol. 7 (2017) 3785−3790.

[17] R. Guo, Y. Qin, L. Qiao, J. Chen, X. Wu, Y. Yao, Catal. Commun. 88 (2017) 94−98.

[18] Y. Dong, S. Huang, S. Wang, Y. Zhao, J. Gong, X. Ma, ChemCatChem 5 (2013) 2174–2177.

[19] Y. Yamamoto, T. Matsuzaki, S. Tanaka, K. Nishihira, K. Ohdan, A. Nakamura, Y. Okamoto, J. Chem. Soc. Faraday Trans. 93 (1997) 3721–3727.

[20] L. Bullot, B. Mulot, A. Simon-Masseron, T.J. Daou, G. Chaplais, J. Patarin, Microporous Mesoporous Mater. 210 (2015) 194–198.

[21] Q. Mou, N. Li, S. Xiang, Microporous Mesoporous Mater. 212 (2015) 73–79.

[22] J. Dhainaut, T.J. Daou, A. Chappaz, N. Bats, B. Harbuzaru, G. Lapisardi, H. Chaumeil, A. Defoin, L. Rouleau, J. Patarin, Microporous Mesoporous Mater. 174 (2013) 117–125.

[23] T. Bécue, J. Manoli, C. Potvin, G. Djéga-Mariadassou, J. Catal. 170 (1997) 123–131.

[24] E.J.P. Feijen, J.L. Lievens, J.A. Martens, P.J. Grobet, P.A. Jacobs, J. Phys. Chem. 100 (1996) 4970–4975.

[25] J.L. Lievens, J.P. Verduijn, A.J. Bons, W.J. Mortier, Zeolites 12 (1992) 698–705.

[26] T. Becue, J. Leglise, J.M. Manoli, C. Potvin, D. Cornet, J. Catal. 179 (1998) 90–99.

[27] T.J. Daou, M. Boltz, L. Tzanis, L. Michelin, B. Louis, Catal. Commun. 39 (2013) 10–13.

[28] E.J.P. Feijen, J.A. Martens, P.A. Jacobs, Stud. Surf. Sci. Catal. 101 (1996) 721–729.

[29] D. Gao, A. Duan, X. Zhang, Z. Zhao, H. E, Y. Qin, C. Xu, Chem. Eng. J. 270 (2015) 176–186.

[30] F. Delprato, L. Delmotte, J.L. Guth, L. Huve, Zeolites 10 (1990) 546–552.

[31] E. Ng, D. Chateigner, T. Bein, V. Valtchev, S. Mintova, Science 335 (2012) 70–73.

[32] X. Liu, D. Yi, Y. Cui, L. Shi, X. Meng, J. Energy Chem. 27 (2018) 271–277.

[33] V. Georgieva, A. Vicente, C. Fernandez, R. Retoux, A. Palčić, V. Valtchev, S. Mintova, Cryst. Growth Des. 15 (2015) 1898–1906.

[34] S.L. Burkett, M.E. Davis, Microporous Mater. 1 (1993) 265–282.

[35] H. Awala, J. Gilson, R. Retoux, P. Boullay, J. Goupil, V. Valtchev, S. Mintova, Nat. Mater. 14 (2015) 447–451.

[36] X. Gao, Y. Zhao, S. Wang, Y. Yin, B. Wang, X. Ma, Chem. Eng. Sci. 66 (2011) 3513–3522.

[37] C. Wang, L. Han, P. Chen, G. Zhao, Y. Liu, Y. Lu, J. Catal. 337 (2016) 145–156.

[38] H. Guan, J. Lin, L. Li, X. Wang, T. Zhang, Appl. Catal. B 184 (2016) 299–308.

[39] T.T.H. Dang, M. Bartoszek, M. Schneider, D. Hoang, U. Bentrup, A. Martin, Appl. Catal. B 121–122 (2012) 115–122.

[40] Y. Pukcothanung, T. Siritanon, K. Rangsriwatananon, Microporous Mesoporous Mater. 258 (2018) 131–140.

[41] C. Wang, P. Chen, Y. Li, G. Zhao, Y. Liu, Y. Lu, J. Catal. 344 (2016) 173–183.

[42] T. Biligetu, Y. Wang, T. Nishitoba, R. Otomo, S. Park, H. Mochizuki, J.N. Kondo, T. Tatsumi, T. Yokoi, J. Catal. 353 (2017) 1–10.

[43] J. Zhou, Y. Zhi, J. Zhang, Z. Liu, T. Zhang, Y. He, A. Zheng, M. Ye, Y. Wei, Z. Liu, J. Catal. 377 (2019) 153–162.

[44] N.S. Gould, B. Xu, J. Catal. 342 (2016) 193–202.

[45] J. Zhang, Y. Zhao, M. Pan, X. Feng, W. Ji, C. Au, ACS Catal. 1 (2010) 32–41.

[46] C.L. Padró, E.A. Rey, L.F. González Peña, C.R. Apesteguía, Microporous Mesoporous Mater. 143 (2011) 236–242.

[47] M. Muñoz, M.A. Gallo, A. Gutiérrez-Alejandre, D. Gazzoli, C.I. Cabello, Appl. Catal. B 219 (2017) 683–692.

[48] F. Maugé, A. Sahibed-Dine, M. Gaillard, M. Ziolek, J. Catal. 207 (2002) 353–360.

[49] Z. Li, W. Wang, D. Yin, J. Lv, X. Ma, Front. Chem. Sci. Eng. 6 (2012) 410–414.

[50] E. Ng, J. Goupil, A. Vicente, C. Fernandez, R. Retoux, V. Valtchev, S. Mintova, Chem. Mater. 24 (2012) 4758−4765.

[51] S.T. Homeyer, W.M.H. Sachtler, J. Catal. 117 (1989) 91−101.

[52] Z. Zhang, W.M.H. Sachtler, H. Chen, Zeolites 10 (1990) 784−789.

[53] D. Teschner, J. Borsodi, A. Wootsch, Z. Revay, M. Haevecker, A. Knop-Gericke, S.D. Jackson, R. Schloegl, Science 320 (2008) 86−89.

[54] J. Zhou, Z. Lou, K. Yang, J. Xu, Y. Li, Y. Liu, S.A. Baig, X. Xu, Appl. Catal. B 244 (2019) 215−224.

[55] C. Wang, Y. Jia, Z. Zhang, G. Zhao, Y. Liu, Y. Lu, Appl. Surf. Sci. 478 (2019) 840−845.

[56] S. Abate, K. Barbera, G. Centi, G. Giorgianni, S. Perathoner, J. Energy Chem. 25 (2016) 297−305.

[57] L.F. Liotta, G.A. Martin, G. Deganello, J. Catal. 164 (1996) 322−333.

[58] O. Dulaurent, K. Chandes, C. Bouly, D. Bianchi, J. Catal. 188 (1999) 237−251.

[59] Y. Fujimori, W.E. Kaden, M.A. Brown, B. Roldan Cuenya, M. Sterrer, H. Freund, J. Phys. Chem. C 118 (2014) 17717−17723.

[60] G. Bistoni, S. Rampino, N. Scafuri, G. Ciancaleoni, D. Zuccaccia, L. Belpassi, F. Tarantelli, Chem. Sci. 7 (2016) 1174−1184.

[61] I. Friberg, N. Sadokhina, L. Olsson, Appl. Catal. B 250 (2019) 117−131.

[62] C. Liu, G. Li, E.J.M. Hensen, E.A. Pidko, J. Catal. 344 (2016) 570−577.

[63] F.E. Celik, T. Kim, A.T. Bell, J. Catal. 270 (2010) 185−195.

[64] J. Lee, Y. Ryou, S.J. Cho, H. Lee, C.H. Kim, D.H. Kim, Appl. Catal. B 226 (2018) 71−82.

[65] S.A. Yashnik, G.A. Urzhuntsev, A.I. Stadnichenko, D.A. Svintsitskiy, A.V. Ishchenko, A.I. Boronin, Z.R. Ismagilov, Catal. Today 323 (2019) 257−270.

[66] Y. Wang, Z. Tao, B. Wu, J. Xu, C. Huo, K. Li, H. Chen, Y. Yang, Y. Li, J. Catal. 322 (2015) 1–13.

[67] O.S.G.P. Soares, L. Marques, C.M.A.S. Freitas, A.M. Fonseca, P. Parpot, J.J.M. Órfão, M.F.R. Pereira, I.C. Neves, Chem. Eng. J. 281 (2015) 411–417.

[68] C. Wang, W. Xu, Z. Qin, S. Mintova, Catal. Commun. 119 (2019) 39–41.